Eur. Phys. J. D **4**, 95–108 (1998)

THE EUROPEAN PHYSICAL JOURNAL D

Optical properties of gold metal clusters: A time-dependent local-density-approximation investigation

J. Lermé[1,a], B. Palpant[1], B. Prével[2], E. Cottancin[1], M. Pellarin[1], M. Treilleux[2], J.L. Vialle[1], A. Perez[2], and M. Broyer[1]

[1] Laboratoire de Spectrométrie Ionique et Moléculaire, CNRS and Université Lyon I, Bâtiment 203, 43 boulevard du 11 novembre 1918, 69622 Villeurbanne Cedex, France
[2] Département de Physique des Matériaux, CNRS and Université Lyon I, Bâtiment 203, 43 boulevard du 11 novembre 1918, 69622 Villeurbanne Cedex, France

Received: 9 March 1998 / Revised: 5 June 1998 / Accepted: 3 July 1998

Abstract. The optical response of free and matrix-embedded gold metal clusters Au_N is investigated in the framework of the time-dependent local-density-approximation (TDLDA). The characteristics of the surface plasmon resonance are carefully analyzed as a function of the model parameters and the particle radius. The strong influence of the frequency-dependence of the 5*d* core-electron dielectric function in the vicinity of the interband threshold is emphasized. The size evolution of the Mie-frequency in free gold clusters exhibits a noticeable blue-shift trend as the particle size decreases, much stronger than in silver clusters. The width and shape of the resonance, essentially ruled by the decay *via* the interband transitions, are found closely correlated to the imaginary component of the core-electron dielectric function. In presence of a surrounding matrix the blue-shift trend is largely rubbed out. Agreement with recent experimental results on size-selected gold clusters embedded in an alumina matrix may be achieved by taking into account the porosity effects at the metal/matrix interface. The comparison with the predictions of classical models is also provided.

PACS. 36.40.-c Atomic and molecular clusters – 71.45.-d Collective effects – 71.45.Gm Exchange, correlation, dielectric and magnetic functions, plasmons

1 Introduction

In the past decade the optical properties of metal clusters have been extensively studied, both experimentally and theoretically [1–4]. This growing interest is motivated by the fruitful information expected to be gained on the electronic structure and the dynamics of the delocalized conduction electrons. Most works have focused on the surface plasmon excitation (the dipolar Mie resonance) which by far dominates the photoabsorption spectra in the near UV/visible range for metal particles of diameter much lower than the wavelength of light [5]. Classically, this resonance corresponds to the collective oscillation of the conduction electron cloud with respect to the ionic background. In the simple model of a free-electron gas embedded in a spherical homogeneous positive charge distribution the surface plasmon frequency is predicted in classical electrodynamics to occur at $\omega_s = \omega_p/3^{1/2}$ where ω_p is the volume plasma frequency (Drude-Sommerfeld model).

In the case of alkali species the finite-size effects are rather strong [6–10]. The surface plasmon frequency moves towards lower energies with decreasing particle size ("red-shift"), and accordingly the polarizability per atom increases [11]. From numerous theoretical investigations devoted to alkali species it is now well established that this behavior has to be attributed to the electron spilling out beyond the ionic background boundary (spillout effect), resulting in a lowering of the average electron density [12]. In spite of the underestimation of the red-shift magnitude the simple Spherical Jellium Model (SJM) [13,14] accounts for the qualitative trends observed in alkali species. Depending on the element better agreement with the experimental findings can be achieved by introducing model refinements such as shape deformations, effective mass corrections, pseudopotentials, core polarization effects or discrete ionic structures.

The interpretation of the optical properties of noble metal clusters is more complex, because the binding energies corresponding to the fully occupied *d*-band are close to those of the *s*-valence band [3,15]. As a consequence, the dynamical response of the valence electrons, responsible for the collective excitations, is strongly influenced by the polarization of the core electrons through screening effects. This screening results in a shift of the volume plasmon, surface plasmon and Mie resonance to lower energies. For instance, assuming that the imaginary component

[a] e-mail: lerme@hplasim2.univ-lyon1.fr

of the metal dielectric function $\varepsilon(\omega) = \varepsilon_{re}(\omega) + i\varepsilon_{im}(\omega)$ does not change much in the region of the resonance, the Mie frequency of large particles is given by $\omega_s = \omega_p/[2\varepsilon_m + \varepsilon^d_{re}(\omega_s)]^{1/2}$. $\chi^d = \varepsilon^d(\omega) - 1$ is the core-electron contribution to the total dielectric susceptibility and ε_m is the dielectric function of the surrounding matrix (assumed to be real).

Optical properties of noble metals, especially silver and gold, have been studied for a long time [3,15]. Most of the early works involved large particles interacting with a surrounding medium (colloidal solutions or matrix-embedded clusters). In spite of some contradictory results [16] most of the experiments are consistent with a blue-shift (matrix-host dependent) as the cluster size decreases. Various effects at the interface, inducing either a blue- or a red-shift, as for instance electron transfer *via* chemical bonding, are thought to be responsible for these discrepancies. Actually very recent investigations on gold clusters in composite systems emphasize the sensitivity of the observed trend or shift magnitude to the interface and the surrounding medium, and – for a given matrix – to the experimental method. For instance Au-doped alumina gel films prepared by a sol-gel technique [17] and SiO_2/Au_N composite films prepared by a sputtering method [18] exhibit a strong red-shift (the average particle diameter is varied by the treatment temperature during the film elaboration), whereas films of Au_N clusters embedded in a porous alumina matrix prepared by codeposition on a substrate show a less pronounced reverse trend [19]. The same behavior (blue-shift) is reported in reference [20] where Au_N gold particles are electrochemically deposited within the cylindrical pores of alumina membranes. However the large sizes involved in this work (16–52 nm) suggest that part of the shift might be due to scattering and higher multipole contributions. A tiny blue-shift trend has been also obtained in dilute solutions of size-selected Au_N clusters passivated by a monolayer of n-alkylthiolates [21].

The blue-shift with decreasing cluster size, illustrated above through various experiments on gold clusters, is a common feature of the other noble metals. The same trend was observed in rare gas/Ag_N and LiF/Cu_N composite thin films [22–24]. The definitive confirmation of the intrinsic nature of the observed size-effects was provided by the photodepletion spectroscopy experiments performed on small free Ag_N^+ and Au_N^+ clusters [25–27]. Nevertheless it is worthwhile noting the determining part played by the charge in the trend governing the size evolution of the surface plasmon frequency [28]. This stems from the large change in the electron density at the surface, namely the compression or spillout increase of the electron cloud for cations and anions respectively.

In this paper we report calculations on the size evolution of the Mie-resonance and polarizability of free and matrix-embedded gold clusters in the range $N = 8-440$. The calculations are carried out in the framework of the time-dependent local-density-approximation (TDLDA) [29–31], within the two-region dielectric model (see Sect. 2.1) introduced recently for studying the optical response of small silver clusters [32]. As compared to silver the main difference concerns the location of the Mie-resonance which lies above the interband threshold ω_{IB}. Although the s and d electrons are treated in a non-equivalent footing the applicability of the model for gold will be demonstrated throughout this paper, mainly in Sections 3.2 and 3.5, through the correct predictions obtained in the large-particle limit (the classical results are recovered) and the good agreement with experimental data. In the case of gold clusters a large broadening of the surface plasmon peak results from the coupling with the absorption from the d-band. With regard to the overall trends and the order of magnitude of the blue-shifts, the results are in good agreement with the recent experiments performed in our laboratory on thin films consisting of gold clusters embedded in an alumina matrix [19]. The striking impact of the energy-dependence of the core electron-related dielectric function $\varepsilon^d(\omega)$ will be pointed out. The influence of some model parameters, as the thickness of the surface- region of reduced polarizability or the matrix porosity, is investigated. Comparison with the predictions of macroscopical classical Mie-like models is also given.

The paper is organized as follows. After a review of previous theoretical investigations on silver clusters, we present in Section 2 the basic ingredients of our calculations, with particular emphasis on the determination of the dielectric function $\varepsilon^d(\omega)$ from the experimental optical constants of bulk gold (Sect. 2.2). The TDLDA results for free and matrix-embedded clusters are given in Section 3, and compared to the classical predictions in Section 3.4. The strong influence of the matrix porosity at the cluster surface is stressed in Section 3.5. The summary of this work is provided in Section 4. Atomic units are used throughout this paper.

2 Theory

2.1 Origin of the blue shift

The physical idea underlying the blue-shift trend observed in noble metal clusters is based on the assumption that – due to the localized character of the core-electron wavefunctions – the screening effects are less effective over a surface layer inside the metallic particle. Close to the surface the valence electrons are then incompletely embedded inside the ionic-core background. In phenomenological dielectric models, this hypothesis is taken into account by assuming that the effective polarizable continuous medium responsible for the screening does not extend over the whole cluster volume, namely by prescribing that $\chi^d(\omega) = \varepsilon^d(\omega) - 1$ vanishes for $r > R - d$ where $R = r_s N^{1/3}$ is the cluster radius and d a thickness parameter on the order of a fraction of the nearest-neighbour atomic distance (r_s is the Wigner-Seitz radius of the bulk metal). This model will be referred to as the two-region dielectric model. This assumption was early introduced by Liebsch to explain the wave-vector dispersion of the Ag-surface plasmon observed in electron energy loss measurements [33]. Assuming that the quantum-mechanical

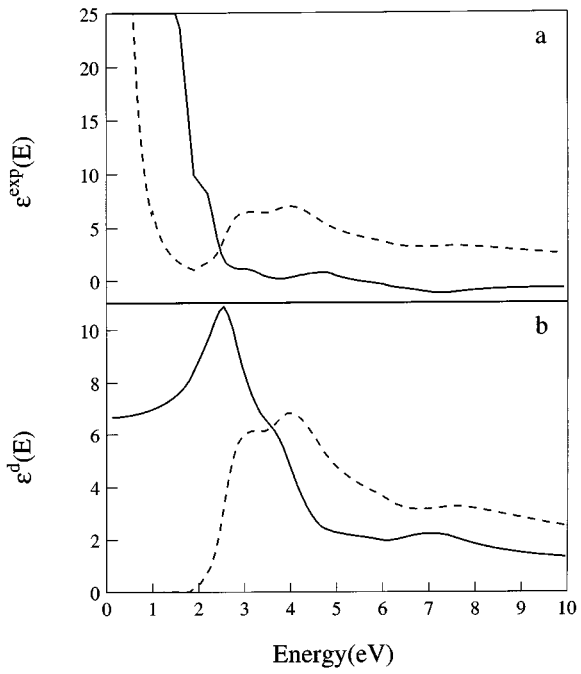

Fig. 1. Spectral dependence of the real (full line curves) and imaginary (dashed line curves) components of the complex dielectric constants of gold metal. (a) Experimental dielectric function $\varepsilon^{exp}(E)$ (the sign of the real part is reversed for convenience) [37]. (b) Bound-electron contribution $\varepsilon^{d}(E)$.

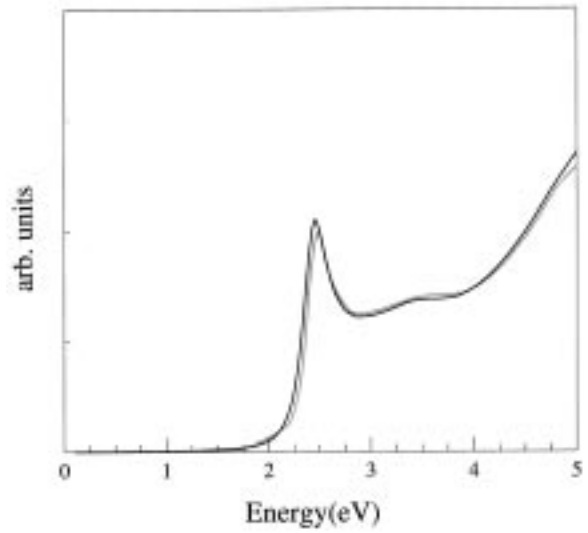

Fig. 2. Mie-absorption spectra of free gold particles (Eq. (4)). Two metal dielectric functions $\varepsilon(E)$ are involved. Grey line curve: experimental dielectric function $\varepsilon(E) = \varepsilon^{exp}(E)$ [37]. Thick line curve: $\varepsilon(E) = \varepsilon^{s}(E) + [\varepsilon^{d}(E) - 1]$.

surface effects are identical for large spherical particles, it was shown that the blue-shift of the Mie-resonance is a consequence of the reduced screening interaction in the surface region. This ingredient was also used within a classical Mie-like model suitable for coated Ag-metal spheres embedded in a rare gas matrix [23]. Subsequently the model was investigated by Kresin within an approximate theoretical formalism [34]. Recently, TDLDA calculations have been performed on free Ag_N and Ag_N^+ clusters in the size range $N \leq 138$, within the two-region dielectric model [32].

A more sophisticated approach has been published during this work, where both the valence and core electrons are microscopically treated [35]. In this formalism, closely related to the one in reference [36] devoted to simple metals in the bulk phase, the dipole moments at each ionic site j, responsible for the screening, are self-consistently determined. The main approximations concern: (i) the ion polarizability $\alpha_j(\omega)$ which is assumed to depend only on the ground-state valence electron density and is computed in an approximate embedded-atom method (in practice, since the valence electron density is rather flat and decreases abruptly at the surface, α_j is taken, either as the free ion polarizability (surface atoms), or as the fully embedded-core polarizability corresponding to the bulk density (inner atoms)), and, (ii) the valence states, and therefore the free response, which are calculated within the simple structureless SJM. Let us point out that the model improvement concerns only the treatment of the influence of the polarizable inner medium on the valence electron response (discrete ionic structure and induced dipolar moments at the ionic sites, and microscopic description of the valence electron-ionic core Coulomb interaction). As in the simple two-region dielectric model [32], the real interband transitions, which dominate the experimental photoabsorption spectra above the Mie resonance, are disregarded in the spectra displayed in Figures 1 and 2 of reference [35] (only the imaginary part of the dynamical valence polarizability – Eq. (18) in Ref. [35] – is calculated). Obviously this refined model, which provides physical support to the phenomenological two-region dielectric model, requires to select a specific geometry and leads to more lengthy computations. Actually calculations involving different cluster geometries yield almost identical results, suggesting that the screening effects do not depend on the details of the ionic frame. Since the two-region dielectric model yields photoabsorption spectra of similar quality – in particular the surface plasmon resonance is located in the same energy range (compare Figs. 1 and 2 in Refs. [32,35], respectively) –, it is expected that applying this more sophisticated microscopical approach would not change much the results reported in this paper.

2.2 Determination of the dielectric function $\varepsilon^{d}(\omega)$

In the model the spherical ionic-core background is phenomenologically described by both, (i) a homogeneous positive charge distribution of radius R and density $\rho_0 = 3/4\pi r_s^3$ (jellium approximation), and, (ii) a continuous homogeneous polarizable medium of radius $R - d$ and complex dielectric function $\varepsilon^{d}(\omega)$. $\varepsilon^{d}(\omega)$ has been extracted from the experimental complex refractive index of bulk

gold [37]. The method is closely related to the one reported in reference [38]. The bulk gold dielectric function $\varepsilon^{exp}(\omega)$ (see Fig. 1a) is decomposed as

$$\varepsilon^{exp}(\omega) = \varepsilon^{s}(\omega) + [\varepsilon^{d}(\omega) - 1] \tag{1}$$

where the free electron contribution $\varepsilon^s(\omega)$ is assumed to be quite well described by the Drude-Sommerfeld model formula

$$\begin{aligned}\varepsilon^{s}(\omega) &= 1 - \frac{\omega_p^2}{\omega(\omega + i\Gamma)} \\ &= \left[1 - \frac{\omega_p^2}{\omega^2 + \Gamma^2}\right] + i\left[\frac{\omega_p^2\Gamma}{\omega(\omega^2 + \Gamma^2)}\right]\end{aligned} \tag{2}$$

where $\omega_p = (\rho_0 q^2/\varepsilon_0 m_{eff})^{1/2}$ is the plasma frequency. The steep low-frequency behaviours of both components $\varepsilon_{re}^{exp}(\omega)$ and $\varepsilon_{im}^{exp}(\omega)$ in Figure 1a are consistent with those deduced from the free-electron gas model equation (2) ($\Gamma \ll \omega_p$). The sudden rise of $\varepsilon_{im}^{exp}(\omega)$ beyond $\omega \approx 1.9$ eV, which reflects the onset of the interband transition $d \to s$, is clear, allowing an unambiguous partition of $\varepsilon^{exp}(\omega)$ into free- and bound-electron contributions. Assuming an effective mass m_{eff} of the conduction electrons equal to unity and $\Gamma = 1/\tau_c$, where τ_c is the conductivity relaxation time at 273 K [39], the imaginary component $\varepsilon_{im}^{d}(\omega)$ is obtained from equations (1, 2) with the additional prescription $\varepsilon_{im}^{d}(\omega \leq 1.8\,\mathrm{eV}) = 0$. Because $\varepsilon_{im}^{s}(\omega)$ is, as compared to $\varepsilon_{im}^{d}(\omega)$, small beyond the interband threshold, the errors resulting from the simple parameterization in equation (2) and the numerical assumptions on m_{eff} and Γ are not important. This does not hold true in respect of $\varepsilon_{re}^{d}(\omega)$ which has moreover to be correctly described in the low-frequency region, where the polarizable medium acts through pure screening effects. Considering that the real and imaginary components of both the total dielectric function $\varepsilon(\omega)$ and $\varepsilon^s(\omega)$ satisfy the Kramers-Kronig relations (due to experimental errors this is not strictly guaranteed for $\varepsilon^{exp}(\omega)$), it follows that $\varepsilon^d(\omega)$ will do too. The real component $\varepsilon_{re}^{d}(\omega)$ is therefore calculated through the formula

$$\varepsilon_{re}^{d}(\omega) = 1 + \frac{2}{\pi} P \int_{\omega_{IB}}^{\infty} \frac{\Omega \varepsilon_{im}^{d}(\Omega)}{\Omega^2 - \omega^2} d\Omega \tag{3}$$

assuming a linear interpolation between consecutive experimental data points. In equation (3) the symbol P stands for the principal value of the integral, and the integration is performed up to 500 eV.

Both components of the dielectric function $\varepsilon^d(\omega)$ are displayed in Figure 1b. In order to validate the previous derivation with regard to our purpose (study of the surface plasmon excitation) a simple numerical test has been carried out. The photoabsorption spectrum of a gold metal sphere has been calculated by the classical Mie theory in the dipolar approximation

$$\sigma(\omega) = 9V\varepsilon_m^{3/2} \frac{\omega \varepsilon_{im}}{(\varepsilon_{re} + 2\varepsilon_m)^2 + \varepsilon_{im}^2} \tag{4}$$

using successively $\varepsilon(\omega) = \varepsilon^{exp}(\omega)$ and $\varepsilon(\omega) = \varepsilon^s(\omega) + [\varepsilon^d(\omega) - 1]$. In equation (4) V is the particle volume. In Figure 2 are displayed the results for free clusters ($\varepsilon_m = 1$). Except for a very tiny shift the agreement is quite good in the spectral region of interest, proving that the Kramers-Kronig relations are quite well satisfied by the experimental dielectric function. In particular the peak maximum location is underestimated by roughly 0.03 eV. This value can be considered as a systematic error in our model calculations.

2.3 Time-dependent local-density-approximation (TDLDA)

Our theoretical framework is the same as the one implicitly involved in reference [32] for free Ag_N clusters. Within the linear-response theory the induced electronic density is expressed as

$$\delta\rho_{ind}(\mathbf{r}, \omega) = \int \chi(\mathbf{r}, \mathbf{r}', \omega) V_{ext}(\mathbf{r}', \omega) d\mathbf{r}' \tag{5}$$

where $V_{ext}(\mathbf{r}, \omega)e^{-i\omega t}$ is the oscillatory external potential ($V_{ext}(\mathbf{r}, \omega) = Z$) and $\chi(\mathbf{r}, \mathbf{r}', \omega)$ is the frequency-dependent density-density correlation function. Within the TDLDA [29–31] it is assumed that the electronic response can be evaluated as in the independent-particle case provided that the induced variation of the ground-state (label gs) mean-field potential $V_{eff}[\mathbf{r}, \rho_{gs}]$ is added to the external one. The induced electron density is thus solution of the self-consistent equation

$$\begin{aligned}\delta\rho_{ind}(\mathbf{r}, \omega) = \int \chi^0(\mathbf{r}, \mathbf{r}', \omega) \Big[& V_{ext}(\mathbf{r}', \omega) \\ & + \int \frac{\delta V_{eff}[\mathbf{r}', \rho]}{\delta \rho}\Big|_{gs} \delta\rho_{ind}(\mathbf{r}'', \omega) d\mathbf{r}'' \Big] d\mathbf{r}'\end{aligned} \tag{6}$$

where $\chi^0(\mathbf{r}, \mathbf{r}', \omega)$ is the independent-electron density-density correlation function and can be expressed in terms of single-particle Green's functions $G(\mathbf{r}, \mathbf{r}', E)$

$$\begin{aligned}\chi^0(\mathbf{r}, \mathbf{r}', \omega) = \sum_i [& \varphi_i^*(\mathbf{r}) \varphi_i(\mathbf{r}') G(\mathbf{r}, \mathbf{r}', \varepsilon_i + \omega) \\ & + \varphi_i(\mathbf{r}) \varphi_i^*(\mathbf{r}') G^*(\mathbf{r}, \mathbf{r}', \varepsilon_i - \omega)]\end{aligned} \tag{7}$$

$G(\mathbf{r}, \mathbf{r}', E) = \langle \mathbf{r}|[H - E - i\delta]^{-1}|\mathbf{r}'\rangle$, where H is the single-particle Kohn-Sham (KS) Hamiltonian. In equation (7) the label i runs over the occupied ground-state KS-wavefunctions φ_i (energies ε_i). In practical calculations a finite δ value is used. In a first approximation this amounts to attributing an intrinsic width 2δ to each bound-bound particle-hole excitation line (Lorentzian-shaped peaks). In most calculations δ was set to a value small enough (30 meV) to resolve the fragmentation pattern resulting from the coupling of the collective mode with the single particle excitations (Landau damping or fragmentation) [40].

The KS mean-field potential in the density functional theory is

$$V_{eff}(\mathbf{r},\rho) = \int V_c(\mathbf{r},\mathbf{r}')[\rho(\mathbf{r}') - \rho_+(\mathbf{r}')]d\mathbf{r}' + v_{xc}[\rho(\mathbf{r})] \tag{8}$$

where $\rho_+(\mathbf{r}) = \rho_0\Theta(R-r)$ is the positive charge distribution (Θ is the Heaviside or step function). $-V_c(\mathbf{r},\mathbf{r}')$ is the classical Coulomb electrostatic potential in the presence of the dielectric media, and $v_{xc}[\rho(\mathbf{r})]$ is the local exchange-correlation potential for which we have invoked the standard Gunnarsson-Lundqvist functional parameterization [41]. From the previous equations it follows that $\chi(\mathbf{r},\mathbf{r}',\omega)$ is determined by the integral equation

$$\chi(\mathbf{r},\mathbf{r}',\omega) = \chi^0(\mathbf{r},\mathbf{r}',\omega) + \iint \chi^0(\mathbf{r},\mathbf{r}_1,\omega)K(\mathbf{r}_1,\mathbf{r}_2)\chi(\mathbf{r}_2,\mathbf{r}')d\mathbf{r}_1 d\mathbf{r}_2 \tag{9}$$

where the driving kernel $K(\mathbf{r}_1,\mathbf{r}_2)$, the so-called residual interaction, arises from the Coulomb electron-electron interaction and exchange-correlation contributions

$$K(\mathbf{r}_1,\mathbf{r}_2) = V_c(\mathbf{r}_1,\mathbf{r}_2) + \left.\frac{dv_{xc}}{d\rho}\right|_{gs}\delta(\mathbf{r}_1-\mathbf{r}_2). \tag{10}$$

The general expression of $V_c(\mathbf{r},\mathbf{r}')$, for both two and three dielectric media (one and two nested spherical interfaces respectively) are given in Appendices A and B.

Note that the dielectric functions, namely the screening effects from the inner polarizable medium and the embedding matrix, are involved in two stages of the calculations: (i) when solving the self-consistent KS-equations for the ground-state problem (the single-particle KS-wavefunctions φ_i and energies ε_i, and consequently the free response χ^0, are thus concerned), and, (ii) in the direct screening of the residual interaction in equation (10). As a matter of fact the direct screening is by far the main factor governing the optical property changes induced by the dielectric media [42,43]. As in all previous calculations we have assumed that the exchange-correlation functional is not modified in the presence of the dielectric media, and moreover takes the same form over the whole energy excitation range, *i.e.* for the ground and excited states [42–44]. Let us stress that an attempt for modifying $v_{xc}[\rho(\mathbf{r})]$, in a way similar to that used for the direct Coulomb interaction, is not straightforward, because the functional parameterization is local. In fact locality prevents any simple procedure from emerging. So far, the validation of this hypothesis as well as its possible influence were never analyzed from a theoretical point of view. Nevertheless, since rather good results are obtained in assuming this approximation – at least in the Mie resonance spectral range – it is expected that the related errors are minor.

The equations considerably simplify for cluster sizes corresponding to closed electronic shells in the ground state, due to the spherical symmetry of the problem. We refer the reader to references [29,30] for more detailed theoretical and technical information. We provide only the fundamental observables calculated in the present work. Once $\chi(\mathbf{r},\mathbf{r}',\omega)$ is calculated by standard matrix techniques the complex induced charge density is obtained through equation (5), and the frequency-dependent complex dynamical polarizability is given by

$$\alpha(\omega) = \int \delta\rho_{ind}(\mathbf{r},\omega)V_{ext}(\mathbf{r},\omega)d\mathbf{r}. \tag{11}$$

The photoabsorption cross-section is given by the imaginary component of the polarizability

$$\sigma(\omega) = 4\pi\omega\mathrm{Im}[\alpha(\omega)]. \tag{12}$$

For large clusters the calculation of TDLDA-absorption spectra requires rather large computational times, due essentially to the large size of the matrixes to be handled for solving the integral equation (Eq. (9))for each ω value. Sum rule formulas, which relate some kth-energy-weighted moments of the strength distribution to simple ground-state properties [12,45,46], have provided efficient numerical accuracy tests.

3 Results

We present now the results of the two-region dielectric model which is thought to describe quite well the size effects in the surface plasmon band of real noble metal clusters. Strictly speaking the thickness d of the region of reduced polarizability is a phenomenological parameter. In view of the approximation consisting in replacing the discrete ionic structure by continuous step-walled jellium and polarizable media, a rigorous rule for setting its value cannot be defined. Nevertheless it is advisable to justify our choice. By comparing the Wigner-Seitz radius r_s of bulk silver with the extent of the electron d-wavefunction Kresin has estimated the thickness parameter d to be about 2 a.u. in Ag_N clusters [34]. Obviously the estimate depends on the threshold for which the d-electron density is regarded as negligible. In TDLDA calculations carried out on the Ag_{59}^+ cluster, assuming $d = 2$ a.u. seems to reproduce quite nicely the experimental photoabsorption spectrum [32]. Moreover this value is of the same order of magnitude as the one used by Liebsch to fit experimental data on Ag surface [33]. We have performed atomic calculations involving nonlocal norm-conserving pseudopotentials [47]. The results show that the tails of the nd-wavefunctions are rather similar for Ag and Au atoms ($4d$ and $5d$ respectively). Since the r_s-values of these two elements are very close ($r_s = 3.02$ a.u. and 3.01 a.u. respectively) [48] the value $d = 2$ a.u. seems to be a reasonable prescription for investigating the optical properties of gold clusters. In order to emphasize the model-parameter dependence, we also provide results obtained with $d = 0$ and 1 a.u. Due to the above-mentioned approximations, involving refinements such as a size-dependent thickness appears to be irrelevant, though the

optical properties of very small Ag_N^+ and Au_N^+-clusters suggest that the reduced-screening region has to be extended probably over the whole cluster volume in this size range [25–27]. This peculiarity stems from the fact that most of the atoms lie at the surface, and moreover that the electron d-related bulk dielectric function is probably not a relevant theoretical concept for very small clusters.

3.1 Qualitative analysis of the size effects

Two main physical ingredients, leading to opposite trends, are responsible for the size evolution of the optical properties in noble metal clusters, namely: (i) the surface region of reduced polarizability which yields a blue shift relative to the bulk limit (see Sect. 2.1), and, (ii) the quantum-mechanical spillout effect which red-shifts the plasmon frequency. It is worthwhile recalling both competing effects within simple physical terms for making the analysis of the raw TDLDA absorption spectra (for both free and matrix-embedded clusters) easier. Let us stress that disentangling the respective numerical contributions to the net resonance-shift stemming from both effects (i) and (ii) cannot be achieved in a rigorous way in microscopical TDLDA calculations, and necessarily would rest on some approximate analytical analysis of the problem. In fact the Fermi wavelength $\lambda_F \approx 3.3 r_s$ is large as compared to the skin thickness d. Hence the effects of both interfaces located at $r = R - d$ and R and of the skin region are closely interdependent. The intricate interplay between both ingredients (i) and (ii) is clearly exemplified by the analytical equation derived by Kresin [34]. This somewhat arbitrary separation is however convenient for providing qualitative intuitive guidelines.

We first discuss the ingredient (i) which can be easily included in a classical approach. Although the influence of the imaginary component ε_{im}^d in gold clusters cannot be neglected, only the real part will be considered here in order to simplify the presentation. Depending on the nature of the ionic background it is useful to define the "screened" surface plasmon frequency

$$\omega_{scr} = \frac{\omega_p}{\left[2\varepsilon_m + \varepsilon_{re}^d(\omega_{scr})\right]^{1/2}} \tag{13}$$

and the SJM-related "unscreened" one $\omega_{uns} = \omega_p/(2\varepsilon_m + 1)^{1/2}$. These frequencies are the bulk limits corresponding to the two extreme cases $d/R \approx 0$ and $d = R$ respectively. For a finite particle size such as $R > d > 0$ it is clear that the surface plasmon frequency will be enclosed by these two limiting values (except if large specific finite-size effects occur) and ruled by the ratio N_{scr}/N where N_{scr} is the number of electrons lying in the inner region $r < R-d$. The classical Mie-like absorption formula appropriate to a coated sphere, which depends only on the volumic ratio $f = [(R-d)/R]^3$ (see Sect. 3.4), supports this statement. In a quantum-mechanical approach the underlying relevant parameter and size-evolution law are not expected to be as simple because the electron density is not step-walled and presents size-dependent surface oscillations. Nevertheless, since the relative influence of the skin region increases as the cluster size decreases, the mean trend over a large size range is expected to be qualitatively similar to the classical behavior. Namely a monotonic evolution of the plasmon frequency from ω_{uns} to ω_{scr} as R increases from $R = d$ to some very large value is predicted to be induced by this first effect.

On the other hand the spillout effect is an intrinsic quantum mechanical effect. Within the SJM the corresponding induced red-shift (relative to ω_{uns}) can be related, thanks to sum-rule formula [12], to the amount of electrons outside the jellium sphere in the ground state. In the two-region dielectric model the magnitude of the red-shift is expected to depend also on the inner electron density profile close to the surface in addition to the electron density beyond the radius R, as for instance in SJM-like models involving local ion-pseudopotentials [49]. As a general rule, the softer the surface electron density, the larger the red-shift. In spite of the absence of quantitative theoretical basis, and noticing that the volume plasma frequency ω_p scales as the square root of the bulk density, it is reasonable to consider "the degree of softness" of the surface electron density tail, or in other words the average surface density, as a suitable criterion for estimating the importance of the induced red-shift. We have carried out calculations on some cluster sizes, assuming a dielectric function ε^d in the range 5–10, and have compared the results with those of the standard SJM. The surface profiles of the mean-field potential and electron-density are found quite identical when $\varepsilon_m = 1$ (except for a very tiny softness increase when $d = 0$), suggesting that the red-shift of the plasmon frequency (relative to the respective bulk limits of both models) will be of similar order of magnitude for free clusters. This result contrasts with the effect arising from a surrounding medium of high refractive index which yields a large increase of the softness of the surface electron density [42,44].

3.2 Free clusters

In Figure 3 are displayed photoabsorption spectra exemplifying our TDLDA results over the entire studied size range. The size evolution of the photoabsorption cross-section is clearly evidenced. We discuss successively the various features of the spectra.

3.2.1 Mie-resonance location

Concerning the location of the surface plasmon frequency the interpretation is straightforward in view of the previous qualitative analysis. One observes a blue-shift trend as the cluster size (d-value) decreases (increases). This demonstrates that the influence of the surface region of reduced polarizability overcomes the spillout effects in gold clusters. As indicated above (end of Sect. 3.1) similar mean-field and electron density surface profiles are obtained within the two-region dielectric model and the SJM. The lowering of the plasmon frequency due to the inner dielectric medium, as compared to the SJM

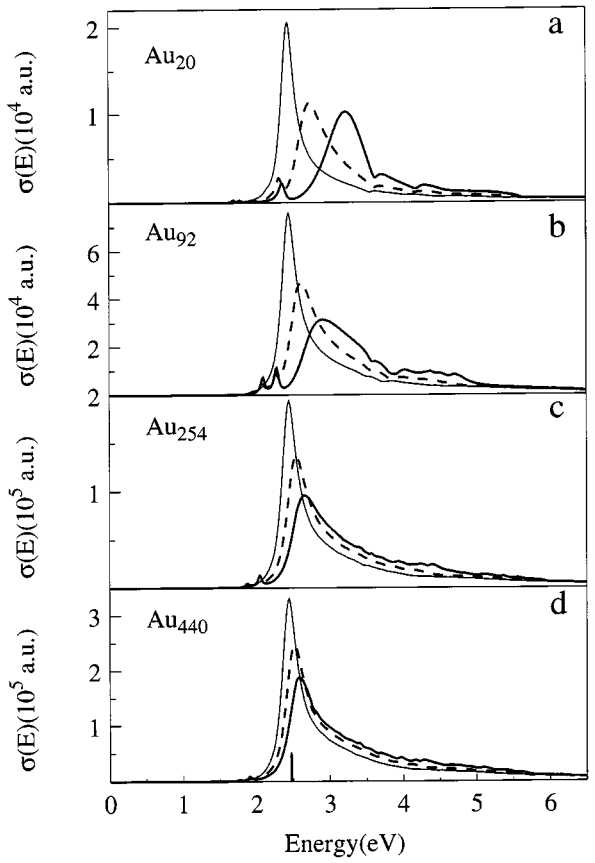

Fig. 3. Photoabsorption spectra of free gold clusters within the two-region dielectric model, for different thicknesses of the skin region of reduced polarizability. Thick line curves: $d = 2$ a.u.; dashed line curves: $d = 1$ a.u.; thin line curves: $d = 0$. The short vertical line in Figure 3d indicates the dipolar Mie-resonance energy in the large-particle limit.

($\omega_s = \omega_p/3^{1/2} \approx 5.21$ eV) is thus entirely governed by the dynamical screening, namely by the residual interaction $K(\mathbf{r}_1, \mathbf{r}_2)$ (Eq. (10)).

A more detailed analysis is however required to explain the surprising size-independence of the plasmon frequency for $d = 0$ a.u. Interpretation of this feature will point out the striking influence of the energy-dependence of $\varepsilon^d(\omega)$ in the region of the collective excitation. Classically the photoabsorption cross-section shows a resonance behaviour when $|\varepsilon(\omega) + 2\varepsilon_m|$ is minimum. Owing to the ω-dependence of ε_{im} this condition is in fact only approximate (see Eq. (4)). Assuming a minimum value equal to zero and solving the corresponding equation in the complex plane allows to infer the $\varepsilon^d(\omega)$-dependence of the main characteristics of the plasmon resonance. Neglecting the damping constant ($\Gamma \ll \omega_s$) in equation (2) the complex plasmon frequency ω^*, whose the real and imaginary components are related to the resonance location and width respectively, is given by the following implicit equation

$$\omega^* = \frac{\omega_p e^{-i\frac{\phi(\omega)}{2}}}{\{[2\varepsilon_m + \varepsilon^d_{re}(\omega^*_{re})]^2 + [\varepsilon^d_{im}(\omega^*_{re})]^2\}^{1/4}} \tag{14}$$

$$\tan\phi = \frac{\varepsilon^d_{im}(\omega^*_{re})}{2\varepsilon_m + \varepsilon^d_{re}(\omega^*_{re})}\,. \tag{15}$$

Since $2\varepsilon_m + \varepsilon^d_{re}(\omega) > \varepsilon^d_{im}(\omega)$ below 4 eV (the ratio is equal to 5 near 2.5 eV), the angle $\phi/2$ is small and approximate values of the real and imaginary components are obtained

$$\omega^*_{re} = \frac{\omega_p}{\{[2\varepsilon_m + \varepsilon^d_{re}(\omega^*_{re})]^2 + [\varepsilon^d_{im}(\omega^*_{re})]^2\}^{1/4}} \approx \frac{\omega_p}{[2\varepsilon_m + \varepsilon^d_{re}(\omega^*_{re})]^{1/2}} \tag{16}$$

$$\omega^*_{im} = -\frac{\varepsilon^d_{im}(\omega^*_{re})}{2[2\varepsilon_m + \varepsilon^d_{re}(\omega^*_{re})]}\omega^*_{re}. \tag{17}$$

In spite of the somewhat artificial derivation of equation (14) the qualitative *and quantitative* information brought by equations (16–17) are quite correct. For instance solving equation (16) leads to the result $\omega^*_{re} = 2.5$ eV which is almost exactly the location of the peak maximum in the Mie-absorption spectrum (see Fig. 2). From the examination of Figure 1 and equation (16) one deduces at once that the Mie-resonance shift trend (red- or blue-shift) and its magnitude are strongly dependent on the location of the large-particle-limit resonance frequency ($\omega_s(\infty)$) relative to the maximum of the steep peak in $\varepsilon^d_{re}(\omega)(\omega_{max})$. If $\omega_s(\infty) < \omega_{max}$, the red (blue)-shift induced by the spillout effect (skin region of reduced polarizability) is counterbalanced by the decrease (increase) of the denominator in equation (16). The net result depends on the slope of the $\varepsilon^d_{re}(\omega)$-curve. Conversely, if $\omega_s(\infty) > \omega_{max}$ the red- and blue-shift trends will be magnified. In the present case $\omega_s(\infty)$ is equal to 2.46 eV, value very close to ω_{max}. Consequently one expects that any "attempt" for a red-shit by finite-size effects will be strongly quenched. This "locking" phenomenon explains both the noticeable blue-shift obtained with $d \geq 1$ a.u. and the quasi size-independence of the Mie-frequency for $d = 0$, specific case where only the spillout effect is present. Actually this phenomenon is responsible for the rather flat size-evolution of the Mie-frequency in Ag_N^+ clusters within the two-region dielectric model. The ω_{max}-value, which is closely related to the interband-threshold through the Kramers-Kronig relations, is located above $\omega_s(\infty)$ in the case of silver metal. We have extended the calculations of reference [32] over the size-range [138–440] and found a similar flat evolution. Actually the most part of the tiny blue-shift results from the charge effect (decrease of the electron spillout for cations).

Figure 4 summarizes the results we obtained over the entire size range. For both the normalized static polarizability $\alpha(N, \omega = 0)/R^3$ (Fig. 4a) and the plasmon peak maximum $\omega_s(N)$ (Fig. 4b) a roughly-linear mean evolution on the $1/R$ scale is found. One observes, as expected

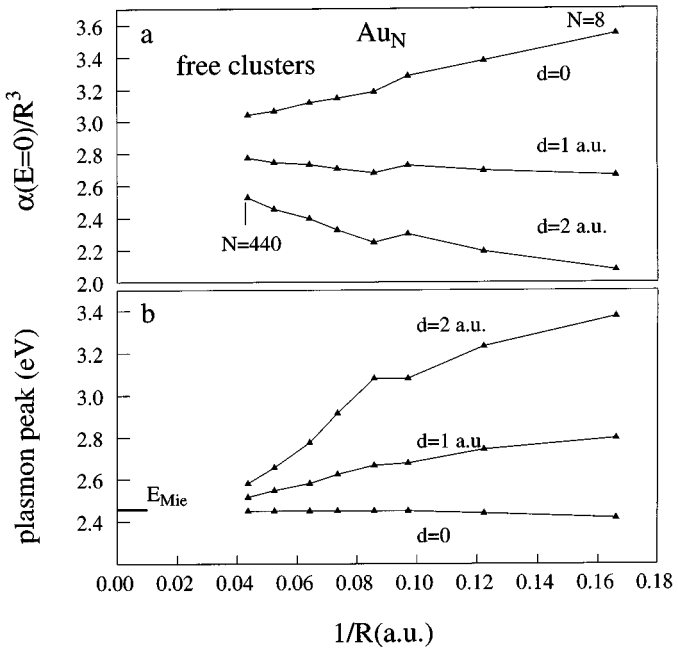

Fig. 4. The size evolution of the normalized static polarizability (a) and of the maximum of the Mie-resonance peak (b) for free gold clusters within the two-region dielectric model, for different d-values. E_{Mie} is the surface plasmon energy in the large-particle limit.

physically, a systematic opposite size-trends in the corresponding curves. However, in contrast with standard SJM results [1,2], one can notice that the "anti-correlation" is less obvious. For instance for $d = 0$, to the flat evolution of $\omega_s(N)$ corresponds a noticeable blue-shift trend in the $\alpha(N, \omega = 0)/R^3$ curve, and, for $d = 2$ a.u., the normalized polarizability evolves much less steeply than the Mie resonance, contrary to SJM results. This peculiarity stems from the large width and the strong asymmetrical shape of the Mie-resonance band (see Fig. 3), resulting in a large breakdown of the so-called surface plasmon-pole formula obtained in assuming that the oscillator strength distribution is exhausted by the collective mode centered at ω_s (namely $\alpha/R^3 = 1/r_s^3\omega_s^2$, deduced from both sum-rule formula $\int \sigma(\omega)d\omega = 2\pi^2 N$ and $\int \sigma(\omega)\omega^{-2}d\omega = 2\pi^2\alpha(\omega = 0)$).

The correct prediction in the large-particle limit, which has to coincide with the classical result, gives support to the suitability of the two-region dielectric model in the case of gold, as for silver. The extrapolation to large sizes of the curve corresponding to $d = 0$ in Figure 4b clearly converges toward the classical Mie prediction 2.46 eV (see Fig. 2). One can notice however that the extrapolation of the curves corresponding to $d = 1$ and 2 a.u. seem to slightly underestimate the classical value. This feature is a consequence of the ω-dependence of $\varepsilon^d(\omega)$, which makes the size evolution on a $1/R$ scale not perfectly linear, contrary to usual SJM results.

3.2.2 Width and shape of the resonance

As it was observed in the case of matrix-embedded potassium clusters [42,43] the collectivity of the Mie excitation increases considerably and the fragmentation phenomenon due to the Landau damping is less developed in the presence of an inner dielectric medium. For $d = 2$ a.u. the Landau fragmentation is reflected through some peaks in the left side of the Mie-band and tiny modulations on the high-energy tail of the spectrum. These features, which are obscured by the coupling with the core-electron absorption band ($\omega_s > \omega_{IB}$), are supported by calculations on Ag_N clusters. In the case of silver the absorption spectra display either a single narrow peak (a small δ-value is involved in the Green's function; see Sect. 2) or a strongly congested multi-peak pattern around the Mie-frequency ($\omega_s < \omega_{IB}$ for silver). The large broadening of the Mie-band in Figure 3 results mainly from the coupling of the collective mode with: (i) the $1p - 1h$ continuum states in the high-energy region (the first continuum threshold lies in the energy-range 3.5–4 eV), and, (ii) the d-electron absorption band ($\omega_{IB} = 1.8$ eV). SJM calculations show that the broadening of the Mie-resonance by the interaction with the $1p - 1h$ continua is reduced as the size increases. This feature holds probably in the presence of the inner dielectric medium. This strongly indicates that the saturation phenomenon in the band-width and shape observed for large sizes has to be attributed to the damping mechanism (ii), in others words the plasmon decay *via* the interband transitions. An estimate from Figure 3d ($d = 0$ (thin curve)) yields the approximate value $\Gamma_{IB} \approx 0.28$ eV (estimate at half-maximum). Moreover additional calculations have proved that the overall width does not depend noticeably on the model-parameter δ involved in the Green's functions (Sect. 2), except for very large values. In particular both the maximum and the degree of asymmetry of the Mie band are found unchanged as δ increases. These features, which cannot be interpreted in terms of a mere spectrum smoothing, suggest that the width and shape of the Mie resonance are mainly ruled by the ω-dependent background-dielectric function $\varepsilon^d(\omega)$. This statement is assessed by estimating $|\omega^*_{im}|$ (Eq. (17)), interpreted as the damping constant Γ_{IB} characterizing the decay *via* the interband transitions. Using the value $\omega^*_{re} = 2.5$ eV one obtains $|\omega^*_{im}| = 0.26$ eV. The numerical consistency between the characteristics of the TDLDA plasmon band (location and width) in Figure 3d with the approximate classical results equations (16, 17) provides an additional support to the present model for studying the size effects in the Mie band of gold nanoparticles. In the energy range 1.8–3.5 eV, especially around 2.5 eV, the relative change in $\varepsilon^d_{im}(\omega)$ is larger than in $\varepsilon^d_{re}(\omega)$. From equation (17) we infer that the size-evolution of the width of the Mie-resonance is closely correlated to the magnitude of $\varepsilon^d_{im}(\omega_s(N))$. The analysis of the spectra in Figure 3 and of $\varepsilon^d(\omega)$ in Figure 1b confirms this assumption. With regard to the resonance profile the observed asymmetry is correlated with the ω-dependence of $\varepsilon^d_{im}(\omega)$ on both sides of $\omega_s(N)$. Namely, the spreading of the collective mode on the energy scale, induced by the coupling with the

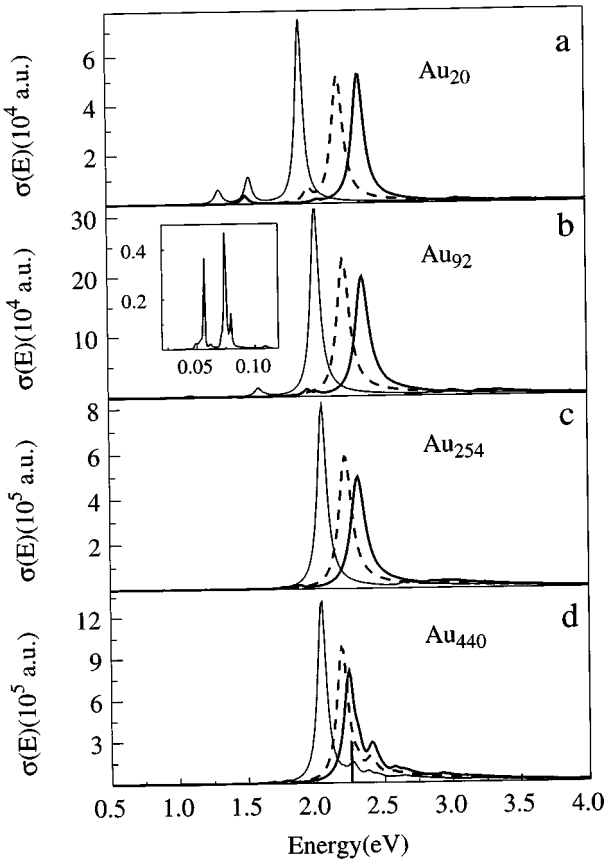

Fig. 5. Photoabsorption spectra of alumina matrix-embedded gold clusters within the two-region dielectric model, for different thicknesses of the skin region of reduced polarizability. Thick line curves: $d = 2$ a.u.; dashed line curves: $d = 1$ a.u.; thin line curves: $d = 0$. The short vertical line in Figure 5d indicates the dipolar Mie-resonance energy in the large-particle limit.

interband transitions, reflects the oscillator strength distribution of the core-electrons excitations.

3.3 Embedded clusters

For comparison purpose with experimental findings we present the results obtained for alumina-embedded Au_N clusters. The theoretical framework is similar to the one used for free clusters, except for the change of the two-body Coulomb interaction $V_c(\mathbf{r}, \mathbf{r}')$ (Appendix B). As in previous works on potassium and silver clusters [42,43] we assume that the effects of the (quasi)-transparent matrix can be mimicked by involving a continuous isotropic medium extending down to the cluster radius R, and characterized by the experimental complex dielectric function $\varepsilon_m(\omega)$ of bulk alumina (ε_m is real and almost constant in the plasmon region and close to the value 3.1) [37].

Concerning the ground state mean-field KS-potential, the matrix effects result in both: (i) a slight up-shift of the potential bottom, and, (ii) a large softness increase of the surface profile. This last feature, which stems from the large matrix-induced charge screening, leads to a much larger electron spillout. The red-shift trend of the plasmon frequency will be then more pronounced compared to free clusters. Since the detailed analysis in Section 3.2 applies to embedded clusters also, we only comment the main modifications induced by the surrounding matrix and exemplified in Figure 5. First one observes a lowering of the large-particle-limit plasmon frequency. The change is tiny because $\varepsilon_m \ll \varepsilon^d$ in the energy range of interest. Assuming the value $\varepsilon_m = 3.1$, equation (16) leads to the result $\omega^*_{re} = 2.25$ eV in perfect agreement with the plasmon frequency obtained in microscopical TDLDA calculations. This value is close to ω_{IB} and consequently the collective mode will be less broadened by the coupling with the interband transitions. With $\omega^*_{re} = 2.25$ eV, equation (17) yields the damping constant $\Gamma_{IB} = |\omega^*_{im}| = 0.065$ eV, value very close to the peak-width in Figure 5d (thin line curve). This agreement emphasizes again the applicability of the present model for gold. Obviously comparison with experimental spectra requires to take into account other sources of resonance broadening. Let us quote the coupling with the thermal fluctuations of the surface [50], the shape-induced resonance splitting [8], the electron scattering at the lattice defects and against the rough surface [3], or the chemical interface damping [51]. As previously stated the collectivity of the Mie excitation is enhanced and the Landau damping is considerably reduced in the presence of a surrounding medium. Except for the smallest size studied ($N = 8$) most part of the oscillator strength ($\int \sigma(\omega) d\omega = 2\pi^2 N$) is exhausted by a single peak, namely the collective Mie resonance.

With regard to the size evolution of the plasmon frequency Figure 6 shows that the surrounding matrix leads to strong effects and modifies quantitatively, *and qualitatively*, the free-cluster size-behaviours (see Fig. 4). The changes are easily interpreted as resulting from the large spillout increase (magnification of the red-shift trend as the cluster size decreases) taking into account the "locking" phenomenon described in Section 3.2.1. In particular, for $d = 2$ a.u. the rather large blue-shift trend in Figure 4 is almost rubbed out, as in the TDLDA results on free Ag_N clusters [32]. For very small clusters better agreement with experiment could be achieved by introducing a larger thickness parameter d [25–27]. With regard to medium and large clusters we will see in Section 3.5 that the matrix porosity effects are probably responsible for the (slight) underestimation of the blue-shifts.

The matrix influence is indeed more spectacularly reflected in the large magnitude of the polarizability (enlargement by a factor on the order of 3–4, see Fig. 6a). These very large values, in view of the rather minor changes of the Mie-frequencies, seem apparently inconsistent with the plasmon-pole formula (see the end of Sect. 3.2.1) which is expected to be satisfied more accurately owing to the plasmon-peak narrowing. Since the f-sum rule is found to be quite well exhausted by the plasmon resonance, the sum-rule $\int \sigma(\omega)\omega^{-2} d\omega = 2\pi^2 \alpha(\omega = 0)$ is suspected to be strongly violated.

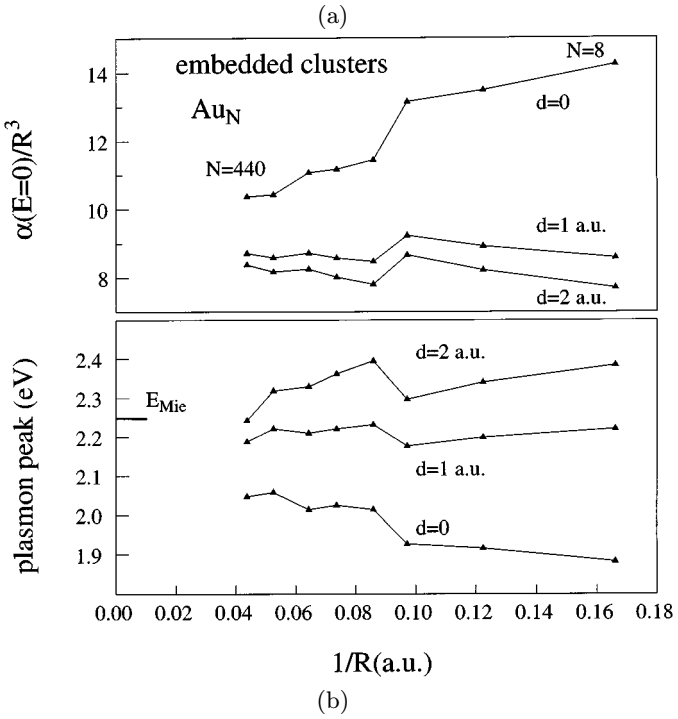

Fig. 6. The size evolution of the normalized static polarizability (a) and of the maximum of the Mie-resonance peak (b) for alumina matrix-embedded gold clusters within the two-region dielectric model, for different d-values. E_{Mie} is the surface plasmon energy in the large-particle limit.

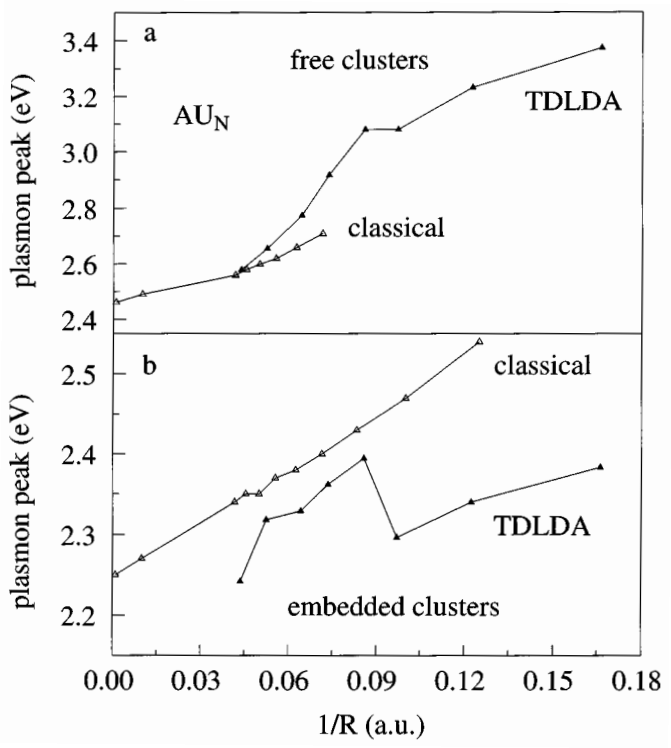

Fig. 7. Comparison of the theoretical surface plasmon frequencies (maximum of the resonance peak) obtained within the classical Mie-theory equation (18) (empty triangles) and the TDLDA formalism (black triangles), in the framework of the two-region dielectric model ($d = 2$ a.u.). (a) Free gold clusters. (b) Alumina matrix-embedded gold clusters.

Actually this intringuing feature is a consequence of the matrix absorption in the far infrared spectral region. The insulating alumina matrix presents very sharp absorption peaks around 0.06 eV. This absorption results in small narrow peaks in the optical response of gold clusters contributing largely to the above sum-rule because of the high value of ω^{-2} (see the inset in Fig. 5b), and therefore invalidates the plasmon-pole formula. From a computational point of view this sum-rule is found satisfied accurately only if the absorption cross-section $\sigma(\omega)$ is carefully estimated in this spectral range (typically the standard energy step $\Delta\omega = 4 \times 10^{-4}$ a.u., used in our TDLDA calculations, has to be reduced by a factor 10). Let us note that these infrared absorption bands are directly responsible for the large decrease of the real part of the dielectric-function $\varepsilon_m(\omega)$ as ω increases from zero to the visible region [37]. In the present work the value corresponding to the lowest tabulated energy value was taken for $\varepsilon_m(0)$, namely $\varepsilon_m(0) = 9.505$. This value is enclosed by the two anisotropic constants $\varepsilon_{11}(= \varepsilon_{22})$ and ε_{33} of the uniaxial Al_2O_3 crystal (in the visible range the anisotropy is less than two percents).

3.4 Comparison with classical results

In this section the microscopic TDLDA results are compared with the classical predictions. The skin region of reduced polarizability is taken into account in using the Mie-like formula appropriate to a coated sphere [3]

$$\sigma(\omega) = 3V\omega\varepsilon_m^{1/2} \times \mathrm{Im}\left\{\frac{(\varepsilon^s-\varepsilon_m)(\varepsilon+2\varepsilon^s)+f(\varepsilon-\varepsilon^s)(\varepsilon_m+2\varepsilon^s)}{(\varepsilon^s+2\varepsilon_m)(\varepsilon+2\varepsilon^s)-f(\varepsilon-\varepsilon^s)(2\varepsilon_m-2\varepsilon^s)}\right\} \quad (18)$$

where the dielectric function ε of the cluster core is equal to $\varepsilon^s(\omega) + [\varepsilon^d(\omega) - 1]$ and $f = [(R-d)/R]^3$ is the ratio of the core to the whole cluster volume. The parameters used are $\Gamma = 30$ meV (Eq. (2)) and $d = 2$ a.u.

The results are displayed in Figure 7, for free (a) and embedded (b) clusters. For small free clusters the peak plasmon is completely rubbed out by the interband transitions, and hence classical predictions are not given in this size range (see Sect. 3.5). As it was stated in Section 3.1 the blue-shift trend induced by the skin region of reduced polarizability is predicted within a simple classical approach. However its magnitude differs noticeably in classical and quantum models. Moreover the discrepancies are not systematic and depend on the physical system which is investigated. For alumina matrix-embedded clusters the TDLDA results are red-shifted relative to the classical ones owing to the large electron spillout effect which is disregarded in a Mie-like classical approach. In the case of free clusters the quantum and classical plasmon frequencies are almost identical in the large-size range.

In the medium- and small-size ranges the TDLDA values are blue-shifted relative to the classical predictions, in spite of the electron spillout. This seemingly contradictory feature stems from the fact that in a quantum model more electrons are beyond the interface of radius $R-d$ and are "associated" with the unscreened plasmon frequency ω_{uns}. In other words the surface electron-density tail, responsible for the spillout effect, leads, *relative to the classical predictions*, to a simultaneous blue-shift trend. The competition between these two opposite trends is ruled by the refractive index of the surrounding matrix.

3.5 Influence of the matrix porosity

How does the cluster-matrix interface influence the optical response of gold metal particles? In view of the various experiments quoted in the introduction, answering confidently this question is undoubtedly a difficult challenge. Informations about the cluster structure, the chemical metal-matrix bonding and the possible charge transfer at the interface are expected to be required [3]. Nevertheless the TDLDA calculations reported in the previous sections have shown that quite reasonable quantitative results can be obtained in the framework of the two-region dielectric model in spherical symmetry. In this paragraph we will show that rather simple dielectric effects may explain the experimental results with a high degree of agreement.

In Figure 8 are displayed experimental findings on composite films consisting of low-concentration ($\leq$ 7%) gold clusters embedded in an amorphous alumina matrix (black squares) [19]. The data correspond to five different particle-size distributions. The mean cluster radius characterizing the samples was calculated through the formula $R_{mean} = \left[\int R^3 f(R) dR\right]^{1/3}$ where $f(R)$ is the normalized particle-radius distribution deduced from transmission electron micrograph analysis. Note that the above definition is more relevant than the formula $\int Rf(R)dR$ since the absorption cross-section is proportional to the number of atoms in the cluster. The experimental data lie between the extrapolated theoretical curves corresponding to free and fully-embedded clusters (empty triangles), suggesting that the experimental results could be explained by taking into account the matrix porosity. Prior to analyzing quantitatively the influence of the porosity let us emphasize that other effects may underlie the discrepancies between the experimental and theoretical results (fully-embedded clusters), as for instance the lattice shrinkage in the small size range [52] (increase of the volume plasma frequency ω_p) or the increase of the thickness parameter d.

Various complementary techniques have pointed out the large porosity of the composite films prepared by co-deposition of both materials on a substrate using the low-energy-cluster-beam-deposition technique. All the results are consistent with a mean porosity of about 45% with respect to crystalline Al_2O_3.

Two kinds of model calculations have been carried out to mimic and quantify the matrix-porosity influence. First, assuming a fine-grained homogeneous porous matrix, calculations with a surrounding medium characterized by a low and constant refractive index, extending down to the cluster surface R, have been performed. Results obtained with $\varepsilon_m = 2$, a value corresponding to a decrease of the matrix polarizability by a factor 2 in the visible spectral range ($\varepsilon_m \approx 3.1$), are shown in Figure 8 (crosses). Despite the quite good numerical agreement for large clusters the slope of the size evolution is noticeably underestimated and the predicted porosity effects would be probably too small for medium and small clusters. Actually the value $\varepsilon_m = 2$, selected for illustration purpose, corresponds to a matrix porosity much more larger. This can be assessed by calculating the dielectric function of the porous alumina matrix using the Bruggeman effective medium theory [53]. The experimentally-determined dielectric function of pure alumina films elaborated under the same deposition conditions as those prevailing during the composite-film preparation provides a more direct support to this assertion. A decrease of roughly 17% with respect to crystalline Al_2O_3 is observed in the visible spectral range ($\varepsilon_m \approx 2.6$). This slight refractive index change would not modify strongly the results corresponding to fully-embedded clusters.

In fact the quantitative failure of the theoretical predictions when fully-embedded clusters are involved is not

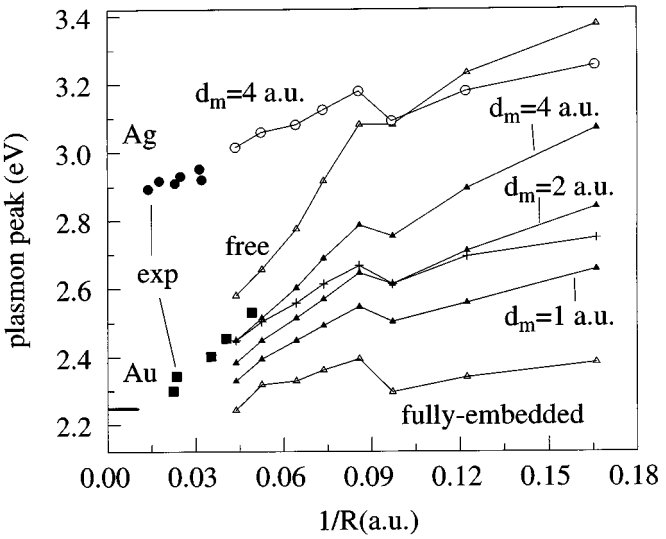

Fig. 8. The size evolution of the surface plasmon energy of gold clusters within different models. Black triangles: TDLDA results obtained with an outer vacuum "rind" at the metal/alumina matrix interface. d_m is the thickness of the outer rind. Empty triangles: TDLDA results for free (upper curve, $d_m = \infty$) and alumina matrix-embedded clusters (lower curve, $d_m = 0$). Crosses: TDLDA results with a homogeneous surrounding matrix characterized by a constant dielectric function $\varepsilon_m = 2$. In all calculations the thickness d of the inner skin of reduced polarizability is equal to 2 a.u. Black squares: experimental results [19]. The short horizontal line at 2.25 eV indicates the surface plasmon energy in the large-particle limit for fully-embedded Au_N clusters. The circles correspond to experimental (black) and TDLDA (empty) results for alumina matrix-embedded Ag_N clusters (model parameters: $d = 2$ a.u. and $d_m = 4$ a.u.).

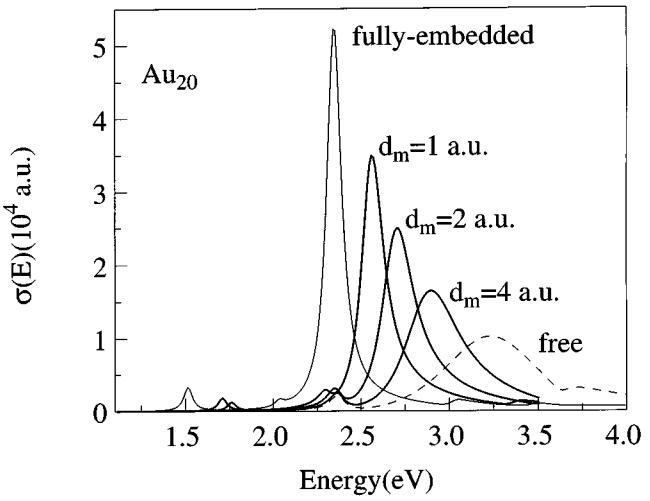

Fig. 9. The evolution of the photoabsorption spectra in presence of an outer vacuum "rind" at the metal/alumina matrix interface. d_m is the thickness of the vacuum rind. Thin line curve: fully-embedded clusters ($d_m = 0$). Dashed line curve: free clusters ($d_m = \infty$).

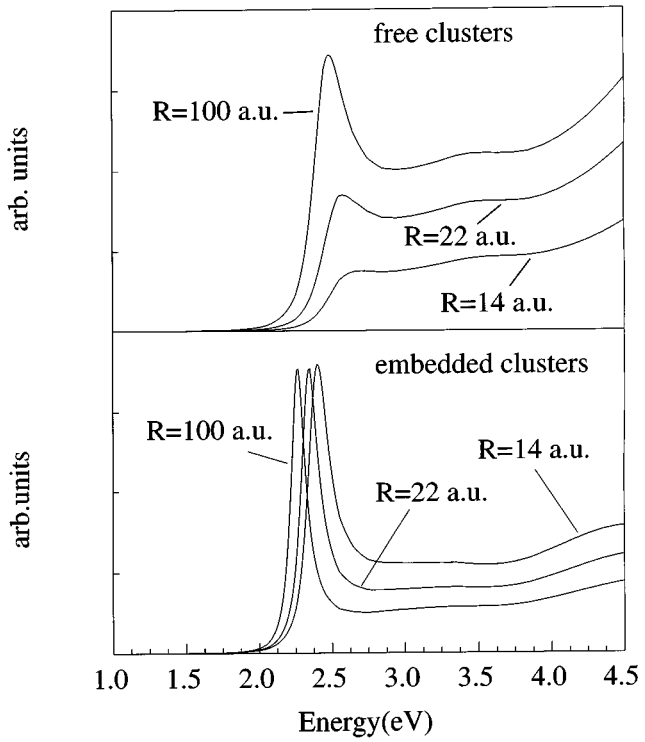

Fig. 10. The size evolution of the photoabsorption cross-section, for free and alumina matrix-embedded gold clusters, calculated within the Mie-theory (Eq. (18)) and $d = 2$ a.u. The various spectra have been independently scaled.

surprising. Since the changes in the electron density $\delta\rho_{ind}$ (Eq. (5)) induced by the oscillating external field are located near the surface it is clear that the short-scale heterogeneity of the porous matrix in the vicinity of the interface will play a crucial part. It is likely that at the cluster/matrix interface the porosity is much more important. The different chemical nature of the constituents and the surface roughness probably implies the existence of defects around the cluster. Hence a more physically-based model would involve a local matrix dielectric function much lower than the large-scale-averaged effective one. Model calculations involving a perfect vacuum "rind" have been carried out ($\varepsilon_m = 1$ in the radial range $R < r < R + d_m$). The change in the Mie-resonance frequency for the thickness values $d_m = 1$ a.u., 2 a.u. and 4 a.u. is exemplified in Figure 9. The size evolutions over the entire studied size range are displayed in Figure 8 (black triangles). As expected the matrix porosity effects are, for a given mean porosity, stronger within this model. One can notice that the discrepancy with the experimental data can be rubbed out with a vacuum-rind thickness d_m much smaller than the Fermi wavelength. Moreover the slope of the curves are in agreement with the experimental size trend. This holds with regard to the shape of the Mie-resonance. In experiment the smaller the mean cluster-radius R_{mean}, the broader and more damped the dipolar resonance. Since the vacuum-rind around the cluster yields a blue-shift of the Mie-resonance frequency the coupling with the interband transitions is much stronger. This results in larger broadening and damping effects (see Fig. 9). Classical calculations involving the formula equation (18) with $d = 2$ a.u., for both free and fully-embedded clusters, illustrate the size evolution of the Mie-resonance shape, which is closely correlated to the blue-shift trend (see Fig. 10). For small and medium free clusters the Mie-resonance is hardly distinguishable from the flat interband-transition contribution. Obviously a comparison with experimental spectra would require to take into account the previously quoted other sources of resonance broadening. Moreover ensemble-averaging over the entire cluster-size distribution of the composite film has to be performed.

The comparison with recent experimental data obtained with Al_2O_3/Ag_N composite films provides evidence for, on the one hand the relevance of the porosity effects, and on the other hand the suitability of the two-region dielectric model for gold and silver. The experimental data for embedded Ag_N clusters are displayed in Figure 8 (black circles). In the beginning of Section 3 it was strongly emphasized that the phenomenological parameter d should be similar for silver and gold. Since the composite films have been elaborated under the same experimental conditions, one expects that the porosity effects should be mimicked by the same parameter d_m. The results of TDLDA calculations on alumina matrix-embedded Ag_N clusters, involving the values $d = 2$ a.u. and $d_m = 4$ a.u., are plotted in Figure 8 (empty circles). The good agreement between theory and experiment, for both silver and gold, in using the same model parameters, proves the suitability of the model for investigating the size effects in the location of the surface plasmon frequency for both metals.

4 Conclusion

In this paper the TDLDA formalism has been applied to study the finite-size effects in the optical response of free and matrix-embedded gold clusters. The polarization, screening and damping effects due to the core electrons and the surrounding medium have been described by means of the complex dielectric functions of the corresponding bulk materials. The calculations have been carried out in the framework of the two-region dielectric model, in which the metallic layer close to the cluster surface is assumed to be less polarizable than the inner region. The competition between the red- and blue-shift trends induced by, respectively, the spillout effect and the skin region of reduced polarizability, is analyzed. The main characteristics of the surface plasmon resonance, as well as the size dependence, have been found closely linked to the energy dependence of the complex dielectric function of the core electrons. In the case of free clusters, the size evolution of the Mie-frequency displays a net blue-shift trend as the cluster size decreases, much stronger than in silver. However, the blue-shift is strongly reduced in presence of a surrounding dielectric medium extending down to the particle surface, due to the increase of the spillout phenomenon. The effect of the matrix porosity at the interface, mimicked by involving a thin vacuum rind between the metal and the embedding matrix, has been investigated. The theoretical results agree quite well with recent experimental data on alumina matrix-embedded gold particles, with respect to both the location and the damping of the surface plasmon resonance.

Appendix A: Two-body Coulomb interaction in presence of dielectric media; case of a single spherical interface

The Coulomb interaction potential $V_c(\mathbf{r}_1,\mathbf{r}_2)$ between two elementary charges located at $\mathbf{r}_1$ and $\mathbf{r}_2$ in presence of a sphere of radius R and dielectric constant ε_1 surrounded by an infinite medium of dielectric constant ε_2 is expressed as [42]

$$\frac{1}{\varepsilon_2}\sum_\ell\left[\frac{r_<^\ell}{r_>^{\ell+1}}+\frac{R^{2\ell+1}}{(r_1r_2)^{\ell+1}}\frac{\ell(\varepsilon_2-\varepsilon_1)}{\ell\varepsilon_1+(\ell+1)\varepsilon_2}\right]P_\ell[\cos(\alpha)] \qquad r_1,r_2>R$$

$$\sum_\ell\left[\frac{r_<^\ell}{r_>^{\ell+1}}\frac{2\ell+1}{\ell\varepsilon_1+(\ell+1)\varepsilon_2}\right]P_\ell[\cos(\alpha)] \qquad r_1<R<r_2 \text{ or } r_2<R<r_1$$

$$\frac{1}{\varepsilon_1}\sum_\ell\left[\frac{r_<^\ell}{r_>^{\ell+1}}+\frac{(r_1r_2)^\ell}{R^{2\ell+1}}\frac{(\ell+1)(\varepsilon_1-\varepsilon_2)}{\ell\varepsilon_1+(\ell+1)\varepsilon_2}\right]P_\ell[\cos(\alpha)] \qquad r_1,r_2<R$$

where the P_ℓ's are the Legendre polynomials, α is the angle between the vectors $\mathbf{r}_1$ and $\mathbf{r}_2$, $r_>=\max(r_1,r_2)$ and $r_<=\min(r_1,r_2)$.

Appendix B: Two-body Coulomb interaction in presence of dielectric media; case of two nested spherical interfaces (radii R_1 and R_2, $R_1<R_2$)

The Coulomb interaction potential $V_c(\mathbf{r}_1,\mathbf{r}_2)$ between two elementary charges located at $\mathbf{r}_1$ and $\mathbf{r}_2$ in presence of a coated dielectric sphere (dielectric constant ε_1 in the radial range $[0,R_1]$, dielectric constant ε_0 in the radial range $[R_1,R_2]$) surrounded by an infinite medium of dielectric constant ε_2 is obtained by solving the Poisson equation with the proper boundary conditions at both interfaces (continuity of the potential and of the normal component of the displacement vector). Six cases have to be considered depending on the values of r_1 and r_2 relative to the interface radii (V_c is symmetric). The derivation of the final expressions is rather tedious and the formulas as a function of the parameters ε_1, ε_0, ε_2, R_1 and R_2 are cumbersome. Hence we provide the various expressions in the closest form, suitable for a straightforward implementation in a numerical code

$$\sum_\ell\left[\frac{A_\ell}{r_2^{\ell+1}}+\frac{1}{\varepsilon_2}\frac{r_<^\ell}{r_>^{\ell+1}}\right]P_\ell[\cos(\alpha)] \qquad r_1,r_2>R_2$$

$$\sum_\ell\left[B_\ell r_2^\ell+\frac{C_\ell}{r_2^{\ell+1}}\right]P_\ell[\cos(\alpha)] \qquad R_1<r_2<R_2<r_1$$

$$\sum_\ell\left[D_\ell r_2^\ell\right]P_\ell[\cos(\alpha)] \qquad r_2<R_1<R_2<r_1$$

$$\sum_\ell\left[E_\ell r_2^\ell+\frac{F_\ell}{r_2^{\ell+1}}+\frac{1}{\varepsilon_0}\frac{r_<^\ell}{r_>^{\ell+1}}\right]P_\ell[\cos(\alpha)] \qquad R_1<r_1,r_2<R_2$$

$$\sum_\ell\left[G_\ell r_2^\ell\right]P_\ell[\cos(\alpha)] \qquad r_2<R_1<r_1<R_2$$

$$\sum_\ell\left[H_\ell r_2^\ell+\frac{1}{\varepsilon_1}\frac{r_<^\ell}{r_>^{\ell+1}}\right]P_\ell[\cos(\alpha)] \qquad r_1,r_2<R_1$$

with

$$B_\ell=-(2\ell+1)[\ell\varepsilon_1+(\ell+1)\varepsilon_0]\left(\frac{R_2}{R_1}\right)^{2\ell+1}\frac{1}{\Delta r_1^{\ell+1}}$$

$$C_\ell=\ell(2\ell+1)(\varepsilon_1-\varepsilon_0)\frac{R_2^{2\ell+1}}{\Delta r_1^{\ell+1}}$$

$$A_\ell=C_\ell+R_2^{2\ell+1}\left[B_\ell-\frac{1}{\varepsilon_2 r_1^{\ell+1}}\right]$$

$$D_\ell=B_\ell+\frac{C_\ell}{R_1^{2\ell+1}}$$

$$F_\ell=\frac{\ell(\varepsilon_1-\varepsilon_0)}{\varepsilon_0}\Big\{(\ell+1)(\varepsilon_0-\varepsilon_2)+[\ell\varepsilon_0+(\ell+1)\varepsilon_2]\left(\frac{R_2}{r_1}\right)^{2\ell+1}\Big\}\frac{r_1^\ell}{\Delta}$$

$$E_\ell=-\frac{1}{\varepsilon_0 r_1^{\ell+1}}-\frac{[\ell\varepsilon_1+(\ell+1)\varepsilon_0]}{R_1^{2\ell+1}}\frac{F_\ell}{\ell(\varepsilon_1-\varepsilon_0)}$$

$$G_\ell=E_\ell+\frac{F_\ell}{R_1^{2\ell+1}}+\frac{1}{\varepsilon_0 r_1^{\ell+1}}$$

$$H_\ell = \left\{ \left[(\ell+1)(\varepsilon_2-\varepsilon_0) - [\ell\varepsilon_0 + (\ell+1)\varepsilon_2] \left(\frac{R_2}{R_1}\right)^{2\ell+1} \right] \times \frac{(2\ell+1)}{\Delta} - \frac{1}{\varepsilon_1} \right\} \frac{r_1^\ell}{R_1^{2\ell+1}}$$

$$\Delta = \ell(\ell+1)(\varepsilon_2-\varepsilon_0)(\varepsilon_1-\varepsilon_0) - [\ell\varepsilon_1 + (\ell+1)\varepsilon_0] \times [\ell\varepsilon_0 + (\ell+1)\varepsilon_2] \left(\frac{R_2}{R_1}\right)^{2\ell+1}$$

References

1. W.A. de Heer, Rev. Mod. Phys. **65**, 611 (1993), and references therein.
2. M. Brack, Rev. Mod. Phys. **65**, 677 (1993), and references therein.
3. U. Kreibig, M. Vollmer, *Optical Properties of Metal Clusters* (Springer, 1995).
4. Comments At. Mol. Phys., Vol. 31, *Nuclear Aspects of Simple Metal Clusters*, edited by C. Bréchignac, Ph. Cahuzac (Overseas Publishers Association, 1995).
5. G. Mie, Ann. Phys. (Leipzig) **25**, 377 (1908).
6. C.R.C. Wang, S. Pollak, T.A. Dahlseid, G.M. Koretsky, M.M. Kappes, J. Chem. Phys. **96**, 7931 (1992).
7. J. Blanc, V. Bonacic-Koutecky, M. Broyer, J. Chevaleyre, Ph. Dugourd, J. Koutecky, C. Scheuch, J.P. Wolf, L. Wöste, J. Chem. Phys. **96**, 1793 (1992).
8. K. Selby, M. Vollmer, J. Masui, V. Kresin, W.A. de Heer, W.D. Knight, Phys. Rev. B **40**, 5417 (1989).
9. C. Bréchignac, Ph. Cahuzac, N. Kebaïli, J. Leygnier, A. Sarfati, Phys. Rev. Lett. **68**, 3916 (1992).
10. T. Reiners, C. Ellert, M. Schmidt, H. Haberland, Phys. Rev. Lett. **74**, 1558 (1995).
11. W.D. Knight, K. Clemenger, W.A. de Heer, W.A. Saunders, Phys. Rev. B **31**, 2539 (1985).
12. Let us point out that the red shift is – basically – a dynamical effect, namely related to the location of the centroid of the surface charge fluctuations, but the sum-rule technique allows to correlate the moments of the oscillator strength distribution, in particular the mean square frequency, to static ground state properties. See for instance P.G. Reinhard, M. Brack, O. Genzken, Phys. Rev. A **41**, 5568 (1990).
13. W. Ekardt, Phys. Rev. B **29**, 1558 (1984).
14. D.E. Beck, Solid State Commun. **49**, 381 (1984).
15. U. Kreibig, L. Genzel, Surf. Sci. **156**, 678 (1985).
16. M.A. Smithard, Solid. State Commun. **13**, 153 (1973).
17. Y. Hosoya, T. Suga, T. Yanagawa, Y. Kurokawa, J. Appl. Phys. **81**, 1475 (1997).
18. I. Tanahashi, M. Yoshida, Y. Manabe, T. Tohda, Surf. Rev. Lett. **3**, 1071 (1996).
19. B. Palpant, B. Prével, J. Lermé, E. Cottancin, M. Pellarin, M. Treilleux, A. Perez, J.L. Vialle, M. Broyer, Phys. Rev. B **57**, 1963 (1998).
20. G.L. Hornyak, C.J. Patrissi, C.R. Martin, J. Phys. Chem. B **101**, 1548 (1997).
21. M.M. Alvarez, J.T. Khoury, T.G. Schaaff, M.N. Shafigullin, I. Vezmar, R.L. Whetten, J. Phys. Chem. B **101**, 3706 (1997).
22. K.P. Charlé, W. Schulze, B. Winter, Z. Phys. D **12**, 471 (1989).
23. S. Fedrigo, W. Harbich, J. Buttet, Phys. Rev. B **47**, 10706 (1993).
24. J. Zhao, H. Zhang, G. Wang, J. Phys. Chem. Solids **57**, 225 (1996).
25. J. Tiggesbäumker, L. Köller, H.O. Lutz, K.H. Meiwes-Broer, Chem. Phys. Lett. **190**, 42 (1992).
26. J. Tiggesbäumker, L. Köller, K.H. Meiwes-Broer, A. Liebsh, Phys. Rev A **48**, R1749 (1993).
27. M. Lindinger, K. Dasgupta, G. Dietrich, S. Krückeberg, S. Kuznetsov, K. Lützenkirchen, L. Schweikhard, C. Walther, J. Ziegler, Z. Phys. D **40**, 347 (1997).
28. J. Tiggesbäumker, L. Köller, K.H. Meiwes-Broer, Surf. Rev. Lett. **3**, 509 (1996).
29. M.J. Stott, E. Zaremba, Phys. Rev. A **21**, 12 (1980).
30. A. Zangwill, P. Soven, Phys. Rev. A **21**, 1561 (1980).
31. W. Ekardt, Phys. Rev. B **31**, 6360 (1985).
32. Ll. Serra, A. Rubio, Z. Phys. D **40**, 262 (1997).
33. A. Liebsch, Phys. Rev. Lett. **71**, 145 (1993); Phys. Rev. B **48**, 11317 (1993).
34. V.V. Kresin, Phys. Rev. B **51**, 1844 (1995).
35. Ll. Serra, A. Rubio, Phys. Rev. Lett. **78**, 1428 (1997).
36. K. Sturm, E. Zaremba, K. Nuroh, Phys. Rev. B **42**, 6973 (1990).
37. E.D. Palik, *Handbook of optical constants of solids*, Vol. I and II (Academic Press Inc., 1985/1991).
38. H. Ehrenreich, H.R. Philipp, Phys. Rev. **128**, 1622 (1962).
39. N.W. Ashcroft, N.D. Mermin, *Solid State Physics* (Saunders College Publishing, Philadelphia, 1988).
40. C. Yannouleas, R.A. Broglia, Ann. Phys. **217**, 105 (1992).
41. O. Gunnarsson, B.I. Lundqvist, Phys. Rev. B **13**, 4274 (1976).
42. A. Rubio, Ll. Serra, Phys. Rev. B **48**, 18222 (1993).
43. Ll. Serra, A. Rubio, Z. Phys. D **26**, S122 (1993).
44. M.J. Puska, R.M. Nieminen, M. Manninen, Phys. Rev. B **31**, 3486 (1985).
45. E. Lipparini, S. Stringari, Phys. Rep. **175**, 103 (1989).
46. O. Bohigas, A.M. Lane, J. Martorell, Phys. Rep. **51**, 267 (1979).
47. G.B. Bachelet, D.R. Hamann, M. Schlüter, Phys. Rev. B **26**, 4199 (1982).
48. C. Kittel, *Introduction to Solid State Physics* (John Wiley and Sons Inc., 1983).
49. J. Lermé, Phys. Rev. B **54**, 14158 (1996).
50. C. Yannouleas, J.M. Pacheco, R.A. Broglia, Phys. Rev. B **41**, 6088 (1990).
51. B.N.J. Persson, Surf. Sci. **281**, 153 (1993).
52. G. Apai, J.F. Hamilton, J. Stohr, A. Thompson, Phys. Rev. Lett. **43**, 165 (1979).
53. D.A.G. Bruggeman, Ann. Phys. (Leipzig) **24**, 636 (1935).